Inorganic Chemistry

ARTICLE

pubs.acs.org/IC

$Ba_4KFe_3O_9$: A Novel Ferrite Containing Discrete 6-Membered Rings of Corner-Sharing FeO_4 Tetrahedra

Qingbiao Zhao,[†] Saritha Nellutla,[‡] Won-Joon Son,[‡] Shae A. Vaughn,[†] Longfei Ye,[§] Mark D. Smith,[†] Vincent Caignaert,[⊥] Michael Lufaso,[¶] Thomas M. Pekarek,[∥] Alex I. Smirnov,[‡] Myung-Hwan Whangbo,[‡] and Hans-Conrad zur Loye*[,†]

[†]Department of Chemistry and Biochemistry and [§]Department of Physics and Astronomy, University of South Carolina, Columbia, South Carolina 29208, United States

[‡]Department of Chemistry, North Carolina State University, Raleigh, North Carolina 27695, United States

[⊥]CRISMAT, UMR 6508, CNRS-ENSICAEN, 6 Bd. Marechal Juin, 14050 Caen, France

[¶]Department of Chemistry and [∥]Department of Physics, University of North Florida, Jacksonville, Florida 32224, United States

Supporting Information

ABSTRACT: Single crystals of a new iron-containing oxide, $Ba_4KFe_3O_9$, were grown from a hydroxide melt, and the crystal structure was determined by single-crystal X-ray diffraction. This ferrite represents the first complex oxide containing isolated 6-membered rings of corner-sharing FeO_4 tetrahedra. Mössbauer measurements are indicative of two tetrahedral high-spin Fe^{3+} coordination environments. The observed magnetic moment (~3.9 μ_B) at 400 K is significantly lower than the calculated spin-only (~5.2 μ_B) value, indicating the presence of strong antiferromagnetic interactions in the oxide. Our density functional theory calculations confirm the strong antiferromagnetic coupling between adjacent Fe^{3+} sites within each 6-membered ring and estimate the nearest-neighbor spin-exchange integral as ~200 K; next-nearest-neighbor interactions are shown to be negligible. The lower than expected effective magnetic moment for $Ba_4KFe_3O_9$ calculated from χT data is explained as resulting from the occupation of lower-lying magnetic states in which more spins are paired. X-band (9.5 GHz) electron paramagnetic resonance (EPR) spectra of a powder sample consist of a single line at $g \sim 2.01$ that is characteristic of Fe^{3+} ions in a tetrahedral environment, thus confirming the Mössbauer results. Further analysis of the EPR line shape reveals the presence of two types of Fe_6 magnetic species with an intensity ratio of ~1:9. Both species have Lorentzian line shapes and indistinguishable g factors but differ in their peak-to-peak line widths (δB_{pp}). The line-width ratio $\delta B_{pp}(\text{major})/\delta B_{pp}(\text{minor}) \sim 3.6$ correlates well with the ratio of the Weiss constants, $\theta_{minor}/\theta_{major} \sim 4$.

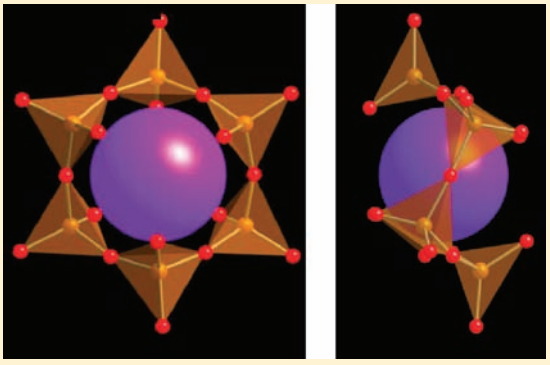

INTRODUCTION

Among extended oxide compounds, structures containing rings of transition metal−oxygen polyhedra are uncommon, with the exception of silicates and germanates, where they are ubiquitous. Natural silicate minerals like beryl and tourmaline have 6-membered rings of corner-sharing SiO_4 tetrahedra,[1] while some germanates, such as $Ge_9O_{19}(OH)_2(N_2C_2H_{10})_2(N_2C_2H_8)_{0.5}\cdot H_2O$, contain both 8- and 11-membered rings of corner-sharing GeO_4 tetrahedra.[2] In contrast, only a small number of iron-containing oxides adopt ring structures. The room temperature $AFeO_2$ (A = K, Rb, and Cs) structures are of the $KGaO_2$ type and contain 6-membered rings of corner-sharing FeO_4 tetrahedra that are connected to adjacent rings by additional corner-sharing.[3] $Na_{14}Fe_6O_{16}$ contains linked 4- and 6-membered rings of corner-sharing FeO_4 tetrahedra,[4] while in $Ba_3NbFe_3Si_2O_{14}$, FeO_4 tetrahedra form trimers that are interconnected via NbO_6 octahedra.[5] Other iron-containing ring structures include $Na_{10}Fe_4O_9$[6] and $Ba_3Fe_2O_6$.[7] In most iron-containing oxides, the rings are interconnected, but exceptions exist, including the tetrahedral trimers in $Ba_3NbFe_3Si_2O_{14}$[5] and the 12-membered rings in $Ba_3Fe_2O_6$.[7]

A number of molecular inorganic ring structures are known[8] and are of interest both for the aesthetics of the structures[9] and for potential applications in catalysis and gas adsorption.[10] Furthermore, when such rings contain magnetic ions, such as manganese, molybdenum, or iron, they typically exhibit complex magnetic interactions.[11] Over the years, a number of iron-containing molecular ring structures, referred to as ferric wheels,[12,13] have been crystallized via solution routes, including $[Fe(OMe)_2(O_2CCH_2Cl)]_{10}$,[13] $[Fe_{14}O_{10}(OH)_4(Piv)_{18}$ (HPiv = pivalic acid),[14] and $[Fe(OH)(C_{30}H_{38}N_2O_8)Fe_2(OCH_3O_4(O_2CCH_3)_2]_6$.[15]

Received: June 27, 2011
Published: September 12, 2011

We have been exploring the crystallization of iron-containing complex oxides using high-temperature solutions, including carbonate and hydroxide melts, and have synthesized complex oxides containing di-, tri-, and tetravalent iron centers.[16,17] Of the fluxes used, the molten hydroxides work especially well for the crystal growth of complex oxides,[18] as noted by other groups that have also investigated the crystal growth of iron-containing oxides out of hydroxide fluxes.[19]

Recently, we succeeded in using hydroxide melts to crystallize a new iron-containing oxide, $Ba_4KFe_3O_9$. To our knowledge, this is the only reported complex iron oxide containing isolated 6-membered rings. We have structurally characterized this new oxide and have collected Mössbauer, electron paramagnetic resonance (EPR), and magnetic data to investigate the magnetic interactions between the iron centers. To supplement these data, we have carried out density functional theory (DFT) calculations to study the magnetic coupling between adjacent iron centers. Herein we report the crystal growth of $Ba_4KFe_3O_9$, its structure determination, and the investigation of its magnetic properties.

EXPERIMENTAL SECTION

Crystal Growth. Single crystals of $Ba_4KFe_3O_9$ were grown from molten hydroxides. In a typical synthesis, 1.9 g of dehydrated $Ba(OH)_2$ [prepared by heating $Ba(OH)_2 \cdot 8H_2O$ (Alfa Aesar, 98%) at 280 °C for 3 h], 2.5 g of KOH (Fisher, reagent grade), and 0.4 g of Fe_2O_3 (Alfa Aesar, 99.998%) were loaded into an alumina crucible, which was then covered with a lid. The crucible was placed in a box furnace, heated to 750 °C over 5 h, held at that temperature for 5 h, cooled to 600 °C over 32 h, and finally cooled to room temperature by turning off the furnace. Upon completion of the reaction, removal of the crucible lid revealed a bed of loose crystals. The crystals were twice washed with 36 mL of isopropyl alcohol under N_2 to remove any remaining flux particles and then, because the crystals are very moisture-sensitive, stored in a glovebox.

Structure Determination. X-ray data from an irregular-shaped black-looking single crystal were obtained at 150(2) K using a Bruker SMART APEX diffractometer (Mo Kα radiation, λ = 0.710 73 Å).[20] The crystal was separated from a rough chunk covered with 1 mL of decane right after the reaction. When thin enough to transmit light, the crystals appear dark brown. The data collection covered 100% of the reciprocal space to $2\theta_{max}$ = 66.3°, with an average redundancy of 23.2 and R_{int} = 0.0995 after absorption correction. Raw area detector data-frame integration was performed with *SAINT+*.[20] Final unit cell parameters were determined by least-squares refinement of 5628 reflections from the data set in the range 6.8° < 2θ < 64.9°. Direct methods structure solution, difference Fourier calculations, and full-matrix least-squares refinement against F^2 were performed with *SHELXTL*.[21]

The compound crystallizes in the cubic space group $Pa\bar{3}$ (No. 205), as determined uniquely by the pattern of systematic absences in the intensity data. There are three barium, two iron, one potassium, three mixed K^+/Ba^{2+}, and six oxygen atom positions in the asymmetric unit. All atoms are in general positions (Wyckoff symbol 24d), except Ba(3), K(1), and K(2)/Ba(2A) (8c, site symmetry 3), K(3)/Ba(3A) (4a, site symmetry $\bar{3}$), and Ba(4)/K(4A) (4b, site symmetry $\bar{3}$). Unreasonably large or small displacement parameters were observed for sites K(2)/Ba(2A) (8c), K(3)/Ba(3A) (4a), and Ba(4)/K(4A) (4b) if refined as fully occupied by Ba^{2+} or K^+, respectively. Trial refinement of the affected site occupancies always showed significant deviations from the unit occupancy by a single atom type. Each site was, therefore, refined as a mixture of Ba^{2+}/K^+, with the total occupancy of each site constrained to the sum of unity. The refined occupancy values are 0.574(3)/0.426(3) for K(2)/Ba(2A), 0.937(5)/0.063(5) for K(3)/Ba(3A), and 0.962(5)/0.038(5) for Ba(4)/K(4A). The occupancies of the other metal atom sites deviated from full occupancy by less than 3% and were not refined. The site mixing model results in a formula of $Ba_{3.97}K_{1.03}Fe_3O_9$. This formula implies a small excess negative charge of 0.03 e^- per formula unit (assuming all Fe^{3+}). This is very close to electroneutrality and supports the site mixing model over a vacancy model. All atoms were refined with anisotropic displacement parameters. The largest residual electron density extrema are +1.88 and −2.07 e/Å located 0.61 and 0.01 Å from Ba(2) and Ba(4)/K(4A), respectively. The reported atomic coordinates were standardized with the *StructureTidy* program implemented in *PLATON*.[22]

Magnetic Susceptibility. The magnetic susceptibility χ of powder samples of $Ba_4KFe_3O_9$ was measured as a function of temperature using a Quantum Design PPMS (San Diego, CA) equipped with a vibrating sample magnetometer attachment. The sample was contained in a gelatin capsule and held in place using small pieces of tissue paper. The capsule was fastened inside a plastic straw that was connected to the PPMS sample holder. $\chi(T)$ values were collected in an applied magnetic field of 1 kG under both field-cooled (FC) and zero-field-cooled (ZFC) conditions. ZFC data were collected in the temperature range of 2−400 K, while FC data were collected in the temperature range of 2−300 K. An empty capsule was prepared in an identical fashion, and its $\chi(T)$ value was collected in order to correct the collected data for the contribution of the sample holder.

Heat Capacity. A representative group of crystals were weighed and placed in an aluminum Tzero sample pan that was coated on the inside with a thin layer of Apiezon N grease to increase thermal contact. The pans were hermetically sealed under helium, which provides further thermal contact with the small crystals. Heat capacity measurements were conducted between 5 and 300 K in zero magnetic field using a Quantum Design PPMS. The lattice contribution was not subtracted from the heat capacity.

Mössbauer Spectra. The ^{57}Fe transmission Mössbauer spectrum was measured at room temperature using a γ-ray source from ^{57}Co embedded in a rhodium matrix. The sample was sealed within two Mylar tapes in a glovebox before measurement. The spectrum was fitted with Lorenzian lines by the *MOSFIT* program. The isomer shift was referenced to metallic α-iron at 293 K.

EPR Spectroscopy. $Ba_4KFe_3O_9$ powder was placed in a 3 × 4 mm (i.d. × o.d.) quartz EPR tube (Wilmad, Vineyard, NJ), filled with nitrogen gas, and flame-sealed. EPR spectra were collected at ∼9.5 GHz (X band) in the 190−360 K temperature range using a Bruker Elexsys 580 spectrometer equipped with an ER4131 variable-temperature unit (all from Bruker Biospin, Billerica MA). Electronic g factors, peak-to-peak line widths (δB_{pp}), and double-integrated intensities (I) were obtained by performing a Levenberg−Marquardt least-squares fitting of the EPR spectra to a two-component model using the *EWVOIGTN* program.[23,24]

RESULTS AND DISCUSSION

Crystal Structure. Single crystals of $Ba_4KFe_3O_9$ were grown out of molten KOH and carefully isolated to prevent exposure to atmospheric moisture to avoid rapid decomposition. Any exposure to moisture causes the structure to visibly degrade, as evidenced by a color change to light brown and the appearance of additional diffraction lines in the powder X-ray diffraction pattern. This extreme moisture sensitivity is likely directly related to this structure type, which contains isolated anionic Fe_6O_{18} rings held in a saltlike environment made up of barium and potassium cations.

The crystallographic data and atomic coordinates are summarized in Tables 1 and 2. The structure consists of a complex

Table 1. Crystal and Refinement Data

empirical formula	$Ba_{3.97}Fe_3K_{1.03}O_9$
fw	897
temperature	150(2) K
wavelength	0.710 73 Å
cryst syst	cubic
space group	$Pa\bar{3}$
unit cell dimens	a = 16.7644(2) Å, α = 90°
	b = 16.7644(2) Å, β = 90°
	c = 16.7644(2) Å, γ = 90°
volume	4711.55(10) Å^3
Z	16
density (calcd)	5.058 Mg/m^3
abs coeff	17.030 mm^{-1}
F(000)	6270
cryst size	0.12 × 0.08 × 0.06 mm^3
θ range for data collection	2.10−33.14°
index ranges	$-25 \le h \le 25$, $-25 \le k \le 25$,
	$-25 \le l \le 25$
reflns collected	104 498
indep reflns	3008 [R(int) = 0.0995]
completeness to θ = 33.14°	100.00%
abs corrn	semiempirical from equivalents
max and min transmn	1.0000 and 0.3407
refinement method	full-matrix least squares on F^2
data/restraints/param	3008/0/108
GOF on F^2	1.078
final R indices [$I > 2\sigma(I)$]	R1 = 0.0314, wR2 = 0.0632
R indices (all data)	R1 = 0.0451, wR2 = 0.0679
extinction coeff	0.000 018(3)
largest diff peak and hole	1.878 and −2.073 e/Å^3

Table 2. Atomic Coordinates ($\times 10^4$) and Equivalent Isotropic Displacement Parameters (Å^2 × 10^3)[a]

	x	y	z	U(eq)	occupancy
Ba(1)	1227(1)	3811(1)	3881(1)	9(1)	
Ba(2)	1359(1)	3712(1)	1374(1)	15(1)	
Ba(3)	3754(1)	3754(1)	3754(1)	12(1)	
Ba(4)	5000	5000	5000	12(1)	0.962(5)
K(4A)	5000	5000	5000	12(1)	0.038(5)
Fe(1)	145(1)	180(1)	2542(1)	8(1)	
Fe(2)	42(1)	2407(1)	2374(1)	8(1)	
K(1)	1236(1)	1236(1)	1236(1)	21(1)	
K(2)	2559(1)	2559(1)	2559(1)	10(1)	0.574(3)
Ba(2A)	2559(1)	2559(1)	2559(1)	10(1)	0.426(3)
K(3)	0	0	0	12(1)	0.937(5)
Ba(3A)	0	0	0	12(1)	0.063(3)
O(1)	2332(2)	4074(2)	2821(2)	14(1)	
O(2)	56(2)	2575(2)	1262(2)	12(1)	
O(3)	1025(2)	2710(2)	2757(2)	13(1)	
O(4)	166(2)	4861(2)	3453(2)	12(1)	
O(5)	1297(2)	2424(2)	4964(2)	12(1)	
O(6)	235(2)	4745(2)	1521(2)	20(1)	

[a] U(eq) is defined as one-third of the trace of the orthogonalized U^{ij} tensor.

cubic barium/potassium framework in which Fe_6O_{18} rings are located. One Fe_6O_{18} ring consisting of corner-shared FeO_4 tetrahedra that encapsulates a potassium ion is shown in Figure 1, left. There are two different tetrahedral iron sites in the ring structure that are arranged such that each Fe(1)O_4 tetrahedron shares one corner with each of the two Fe(2)O_4 tetrahedra and vice versa. The two FeO_4 tetrahedra are slightly distorted, and each has four different Fe−O bond lengths, ranging from 1.83 to 1.89 Å, with O−Fe−O angles from 102.7 to 106.9° (Table 3). The 6-membered ring has a shape similar to the chair conformation of cyclohexane and holds one potassium cation, K(1), in the middle (Figure 1, right). Unlike other FeO_4 tetrahedra-based 6-membered ring structures, the rings in this compound are isolated from each other (Figure 2).

Each Fe_6O_{18} ring has a formal charge of 18−, which is balanced by the Ba^{2+} and K^+ counterions. The ionic radii for 9-coordinate barium and potassium are quite similar, 1.47 and 1.55 Å, respectively. Hence, it is not surprising that some of the counterion sites have mixed Ba^{2+} and K^+ occupancy. The cation site in the middle of the Fe_6O_{18} ring is, however, occupied by potassium only. In this structure, the coordination numbers for Ba^{2+}, K^+, and mixed occupied metal sites range from 9 to 10.

The counterions (Ba^{2+}, K^+, and Ba^{2+}/K^+ mixed sites) form the cubic framework shown in Figure 3, within which the Fe_6O_{18} rings are located. The cation arrangement is best related to a defect body-centered-cubic structure, where the atoms at the corners of the cubes [K(1)] are located in the middle of the ring, while the atoms at the body center of the cubes lie adjacent to the rings. By comparison, in $RbFeO_2$, an oxide with connected 6-membered FeO_4 tetrahedral rings, the Rb^+ counterions arrange in a diamond structure.[25]

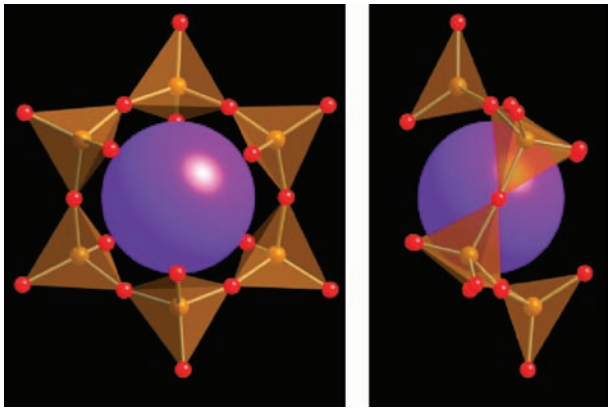

Figure 1. One 6-membered Fe_6O_{18} ring with a potassium atom in the center viewed straight on (left) and sideways (right) to emphasize the chair configuration. FeO_4 tetrahedra are shown in orange, oxygen atoms in red, and potassium atoms in purple.

Mössbauer Spectra, Magnetic Susceptibility, and Heat Capacity. The room temperature Mössbauer spectrum of $Ba_4KFe_3O_9$ (Figure 4) is composed of two quadrupole doublets with isomer shifts and quadrupole splittings (δ_1 = 0.41 mm/s, ΔEQ_1 = 0.64 mm/s and δ_2 = 0.25 mm/s, ΔEQ_2 = 0.55 mm/s) consistent with Fe^{3+} in a high-spin state and a tetrahedral coordination environment.[17] The ratio between these two sites is 0.52/0.48 and is in agreement with the crystal structure. No magnetic hyperfine interactions are observed, consistent with reports for other cyclic iron structures.[12]

dx.doi.org/10.1021/ic201374g |Inorg. Chem. 2011, 50, 10310–10318

Table 3. Selected Bond Lengths (Å) and Bond Angles (deg)[a]

Fe(1)−O(4)#15	1.828(3)
Fe(1)−O(6)#15	1.846(3)
Fe(1)−O(2)#9	1.885(3)
Fe(1)−O(5)#16	1.898(3)
Fe(2)−O(1)#2	1.831(3)
Fe(2)−O(3)	1.840(3)
Fe(2)−O(2)	1.885(3)
Fe(2)−O(5)#16	1.896(3)
O(4)#15−Fe(1)−O(6)#15	124.20(15)
O(4)#15−Fe(1)−O(2)#9	106.19(13)
O(6)#15−Fe(1)−O(2)#9	105.92(15)
O(4)#15−Fe(1)−O(5)#16	105.73(14)
O(6)#15−Fe(1)−O(5)#16	107.95(15)
O(2)#9−Fe(1)−O(5)#16	105.53(13)
O(1)#2−Fe(2)−O(3)	126.48(14)
O(1)#2−Fe(2)−O(2)	102.77(14)
O(3)−Fe(2)−O(2)	106.97(13)
O(1)#2−Fe(2)−O(5)#16	105.23(13)
O(3)−Fe(2)−O(5)#16	105.67(13)
O(2)−Fe(2)−O(5)#16	108.94(14)

[a] Symmetry transformations used to generate equivalent atoms: #1, $-z+{}^1/_2, x+{}^1/_2, y$; #2, $y-{}^1/_2, z, -x+{}^1/_2$; #3, $y, -z+{}^1/_2, x+{}^1/_2$; #4, $-x, y+{}^1/_2, -z+{}^1/_2$; #5, $z, -x+{}^1/_2, y+{}^1/_2$; #6, y, z, x; #7, $x, -y+{}^1/_2, z-{}^1/_2$; #8, $z, -x+{}^1/_2, y-{}^1/_2$; #9, z, x, y; #10, $x+{}^1/_2, y, -z+{}^1/_2$; #11, $-y+1, z+{}^1/_2, -x+{}^1/_2$; #12, $z+{}^1/_2, -x+{}^1/_2, -y+1$; #13, $-x+{}^1/_2, -y+1, z+{}^1/_2$; #14, $-x+1, -y+1, -z+1$; #15, $-x, y-{}^1/_2, -z+{}^1/_2$; #16, $z-{}^1/_2, x, -y+{}^1/_2$.

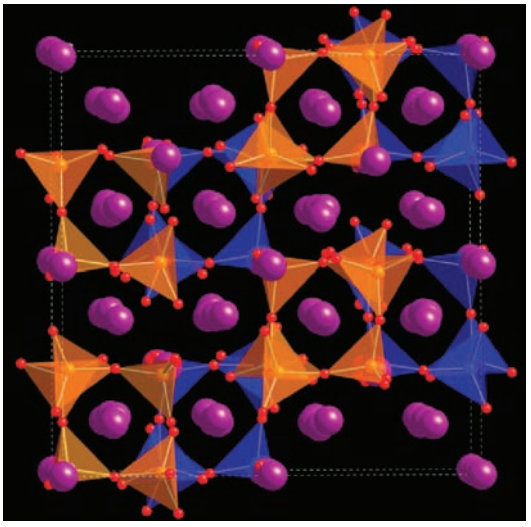

Figure 2. Crystal structure of $Ba_4KFe_3O_9$ depicting the isolated nature of the 6-membered rings. FeO_4 tetrahedra belonging to different rings are shown in orange and blue to illustrate the isolated nature of the rings. Barium and potassium atoms are both shown in purple.

To investigate the possible existence of long-range magnetic order in this oxide, magnetic susceptibility data, $\chi(T)$, were collected between 2 and 400 K. The χ vs T and χ^{-1} vs T plots are shown in Figure 5, which does not contain any feature indicative of a long-range magnetic order. The inverse susceptibility plot is nonlinear over the entire temperature range measured and

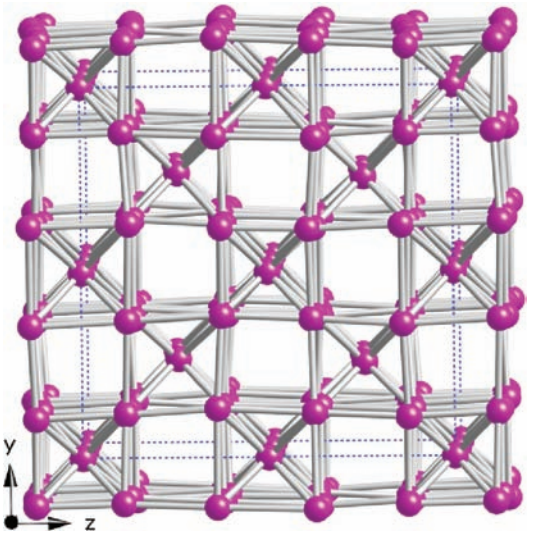

Figure 3. Arrangement of barium and potassium atoms. Barium and potassium atoms are both shown in purple.

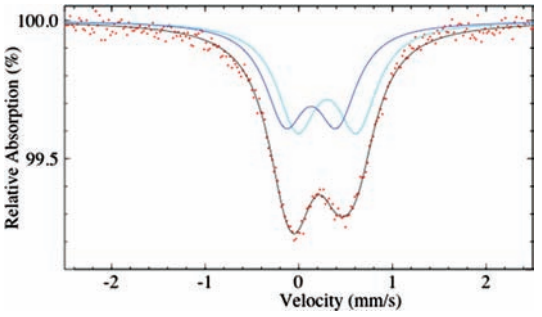

Figure 4. Mössbauer spectrum of $Ba_4KFe_3O_9$.

cannot be readily fit to the Curie law. Furthermore, the χT vs T plot shows a complex change in the moment as a function of the temperature. The observed effective magnetic moment μ_{eff} $[=(8\chi T)^{1/2}]$ of ~3.933 μ_B (Bohr magneton) at 400 K is lower than the expected spin-only value of 5.92 μ_B (for $g = 2$) for a tetrahedral high-spin Fe^{3+} ion. This behavior indicates the presence of antiferromagnetic interactions between Fe^{3+} ions within the Fe_6O_{18} ring. A similar effect was observed for $[Fe_{14}O_{10}(OH)_4(Piv)_{18}]$, where the room temperature moment was only about 20% of the spin-only value.[14]

It has previously been observed that the measured effective magnetic moment is much smaller than the theoretical magnetic moment not only in molecular ring structures but also in related iron and cobalt oxides such as, for example, $BaKFeO_3$[19] and $Ba_3Fe_2O_6$[7] as well as cobalt(IV) compounds Cs_2CoO_3, Rb_2CoO_3, and K_2CoO_3.[26] In some of these cases, it was suggested that the large difference between the observed and theoretical magnetic moments is due to a long-range antiferromagnetic ordering with Néel temperatures above the upper limit of the magnetic measurement temperature.[7,19] It is unlikely that this scenario applies to our system because a long-range antiferromagnetic order was not detected in the Mössbauer spectrum. Nonetheless, in order to investigate the possibility of magnetic order, we collected the heat capacity data shown in Figure 6. The data give no indication of an identifiable magnetic ordering transition between 5 and 300 K.

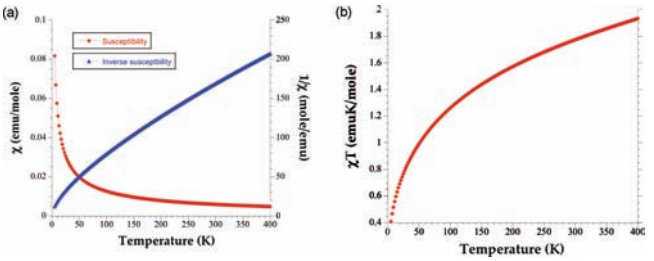

Figure 5. (a) Magnetic susceptibility and inverse susceptibility vs temperature plot per mole of Fe^{3+} for $Ba_4KFe_3O_9$. (b) χT vs temperature plot per mole of Fe^{3+} for $Ba_4KFe_3O_9$.

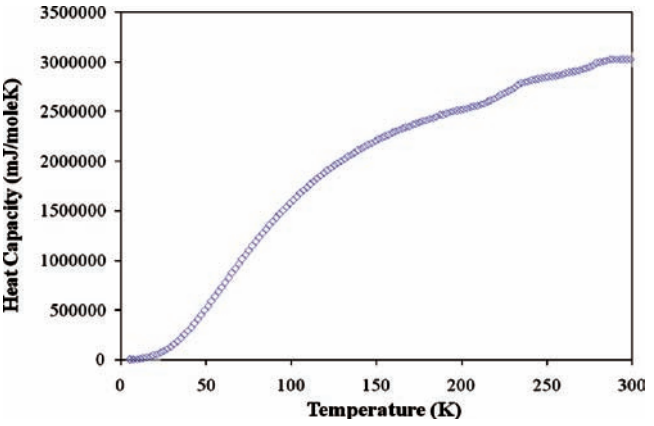

Figure 6. Zero-field heat capacity data for $Ba_4KFe_3O_9$.

EPR Spectroscopy. Figure 7a shows a typical room temperature X-band EPR spectrum from $Ba_4KFe_3O_9$ powder. The spectrum consists of a single line at $g \sim 2.01$, and this g factor is characteristic of a Fe^{3+} ion in a tetrahedral environment.[27,28] The line is sharp at the center but has some broad wings and cannot be fitted to a single Lorentzian line shape (not shown). EPR spectra with broad wings were previously observed for other types of strongly coupled spin systems[29,30] and were explained by either a dipolar broadening model[29] or a two-component Lorentzian model.[30] It was found that $Ba_4KFe_3O_9$ EPR spectra over the entire temperature range studied could be modeled as a superposition of two Lorentzian lines that have the same field position but differ in line widths, with one component by a factor of ~3.6 broader than the other one (see Figure 7a). Note that the number of electronic spins is proportional to the double integral of the corresponding EPR spectrum. Further, for the first derivative, components appear to be of comparable peak-to-peak amplitudes (Figure 7a); for spectra of the same (Lorentzian) shape, such as those shown in Figure 7, the double integral will be proportional to the square of the peak-to-peak width. Then, even though the two components appear to be of comparable peak-to-peak amplitudes (Figure 7a), the double integrated intensity of the broad component represents ~90% of all of the electronic spins because the peak-to-peak width is broader by a factor of ~3.6. Therefore, this component is further referred to as "major", whereas the narrower component, which accounts for the remaining ~10% of the double-integrated intensity, is referred to as "minor". Both components are attributed to Fe^{3+} species based on g factors: $g_{major} = g_{minor} \approx 2.01$. On the basis of the X-ray structure, we assign the major component in the EPR

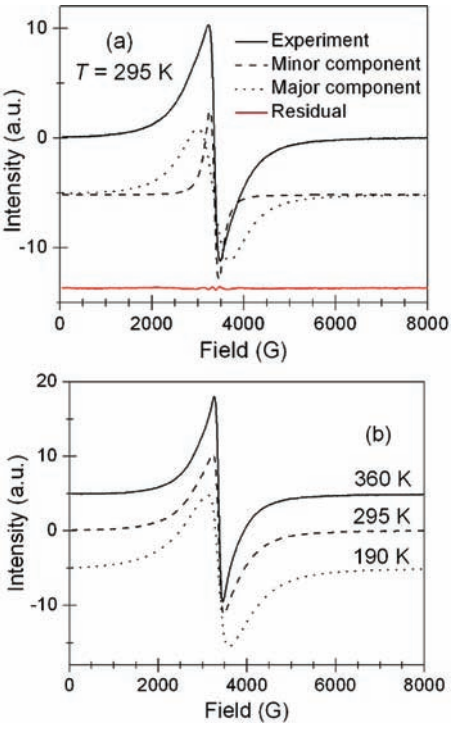

Figure 7. (a) Room temperature X-band EPR spectrum (black solid line) of $Ba_4KFe_3O_9$ powder along with the major (dotted line) and minor (dashed line) components. The fit residual (red solid line), a difference between the experimental and simulated spectra, demonstrates the exceptional quality of the two-component model. The two components and the residual are displaced along the ordinate for clarity. (b) X-band EPR spectra of $Ba_4KFe_3O_9$ powder at three representative temperatures.

spectra to Fe_6 clusters with an encapsulated K^+ ion in the chair conformation.

One may consider the possibility that the two crystallographically distinct tetrahedral Fe^{3+} ions could give rise to the two distinct EPR spectral peaks observed experimentally (Figure 7). However, we believe that this is not the case. X-ray studies show only a single type of Fe_6 ring with two crystallographically distinct Fe^{3+} ions in equal amounts; i.e., each ring is made up of three ions of each type of Fe^{3+} ion. This does not match the 9:1 ratio of the EPR double-integrated intensities. Furthermore, even though the two crystallographically distinct tetrahedral Fe^{3+} ions could yield distinguishable anisotropic EPR spectra for isolated ions, we show that the adjacent Fe^{3+} sites within the 6-membered rings are strongly spin-exchange-coupled. Then, in the limit of strong spin exchange, all of the anisotropic features of Fe^{3+} EPR spectra and, hence, the differences between the EPR spectra corresponding to two crystallographically distinct Fe^{3+} sites would average out, yielding an isotropic Lorentzian shape observed in our experiment. Thus, the presence of the two crystallographically distinct Fe^{3+} sites was ruled out as the origin of the two Lorentzian EPR components. It is more likely that the minor component would originate from a small fraction of a polymorph in the sample or even a partially decomposed sample because of its extreme moisture sensitivity. It is worthwhile to note here that the ability to resolve two components in EPR spectra reinforces the statue of EPR spectroscopy as one of the best analytical tools for detecting and differentiating the electronic spin environments in various systems.

dx.doi.org/10.1021/ic201374g |*Inorg. Chem.* 2011, 50, 10310–10318

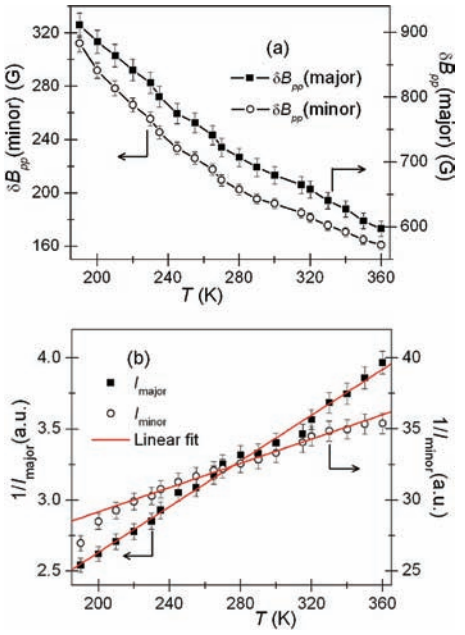

Figure 8. (a) Peak-to-peak EPR line width (δB_{pp}) as a function of the temperature for the major and minor components. The solid lines are guides to the eye. (b) Inverse EPR double-integral signal intensity of the major and minor components as a function of the temperature. The solid red lines are the best linear fit to the Curie−Weiss law. See the text for further details.

To further understand the spin environment in Fe_6 clusters and estimate the nearest-neighbor spin-exchange integral, J_{nn}, we have performed variable-temperature EPR studies from 190 to 360 K (see Figure 7b for representative EPR spectra). Figure 8a shows that the peak-to-peak line width (δB_{pp}) of both the major and minor components decreases monotonously as the temperature increases while maintaining the δB_{pp}(major)/δB_{pp}(minor) ratio of ~3.6. The observed line narrowing with temperature is attributed to further averaging of the local magnetic fields caused by an increased rate of spin fluctuation.

The isotropic exchange integral J can be estimated from $\delta B_{pp}(T)$ according to the Anderson−Weiss (AW) EPR linewidth theory.[31] In a system with strong spin-exchange interactions and containing a uniform distribution of magnetic ions in a simple cubic lattice, the δB_{pp} parameter is related to the dipolar and spin-exchange fields as[31]

$$\delta B_{pp} = \left(\frac{2}{\sqrt{3}}\right)\left(\frac{10B_d^2}{3B_{ex}}\right) \quad (1)$$

$$B_d^2 = 5.1\left(\frac{g\mu_B}{r^3}\right)S(S+1) \quad (2)$$

$$B_{ex} = 1.68\left(\frac{J_{nn}}{g\mu_B}\right)[S(S+1)]^{1/2} \quad (3)$$

where B_d is the dipolar field, B_{ex} is the spin-exchange field, g is the g factor, μ_B is the electronic Bohr magneton, r is the distance between the magnetic ions, S is the spin of the magnetic ion, and k is the Boltzmann constant. Finally, the $^{10}/_3$ factor in eq 1 accounts for additional broadening contributions to the line width from other magnetic interactions such as zero-field splitting from crystal-field interactions and hyperfine interactions.[31]

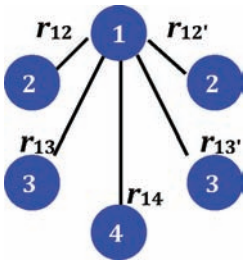

Figure 9. Diagram depicting dipolar interactions considered in estimating the total dipolar field B_d. r_{ij} is the distance between the ith and jth ions and is assumed to be the same for both the minor and major components of $Ba_4KFe_3O_9$. The distances are $r_{12} = r_{12'} = 3.750$ Å, $r_{13} = r_{13'} = 5.642$ Å, and $r_{14} = 6.745$ Å.

Table 4. Curie−Weiss Temperature θ Obtained from the Curie−Weiss Fits (eq 4) of the EPR Intensities as a Function of the Temperature (Figure 8b) and the Nearest-Neighbor Spin-Exchange Integrals J_{nn} Calculated from eq 5[a]

	$I(T)$		$\delta B_{pp}(T)$
	θ (K)	J_{nn} (K)	$\lvert J_{nn}\rvert$ (K)
major component	−125	−21	12
minor component	−470	−81	38

[a] The last column lists the $|J_{nn}|$ values calculated from the AW theory of the EPR line widths (eqs 1−3). The error in θ and J_{nn} is ±5 K.

Let us now assume that the minor component in the EPR spectra originates from a very similar Fe_6 cluster but with different J_{nn} and that these clusters are noninteracting with each other. Because the EPR spectral line shapes of both components of $Ba_4KFe_3O_9$ are Lorentzian, the spin-exchange field in Fe_6 clusters must be sufficiently strong to average out the magnetic anisotropy and local dipolar fields. Therefore, it is reasonable to apply the AW theory to estimate, at least qualitatively, J_{nn} from eqs 1−3. Because our sample contains discrete Fe_6 wheels as opposed to the uniform distribution of Fe^{3+} ions expected in the AW model, we assume that (i) the effective dipolar field B_d at each Fe^{3+} site of the Fe_6 cluster is the sum of dipolar fields due to the remaining Fe^{3+} ions in the Fe_6 cluster (see Figure 9). (ii) The Fe_6 clusters corresponding to the minor and major components have essentially identical bond lengths and angles, resulting in very similar effective dipolar fields B_d. (iii) Because the DFT calculations, vide infra, show that the intraring next-nearest-neighbor interaction $J_{nnn} \ll J_{nn}$, only the two intraring nearest neighbors are considered in calculating J_{nn}. (iv) Note that eqs 1−3 are only valid for the regime of the extreme narrowing of the line width due to large spin-exchange interactions. Thus, only the lowest experimental δB_{pp} values were used for estimating the numerical values of J_{nn}. Table 4 lists the J_{nn} values corresponding to the major and minor components calculated using $g_{major} = g_{minor} \approx 2.01$ and $S_{major} = S_{minor} = {}^5/_2$.

Figure 8b shows a plot of the inverse of the double-integrated EPR intensity (I) as a function of the temperature for both the major and minor components. Notably, I_{major}/I_{minor} remains at ~10 over the entire temperature range, thus, reinforcing the validity of the two-component model. As long as the thermal

dx.doi.org/10.1021/ic201374g |Inorg. Chem. 2011, 50, 10310–10318

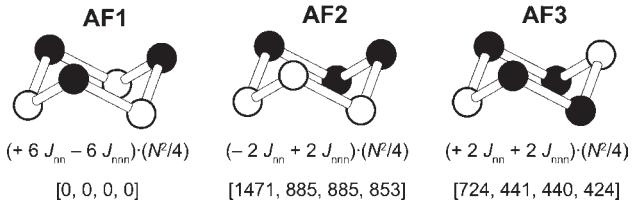

Figure 10. Three ordered spin arrangements of each iron hexamer ring used for the energy-mapping analysis, where the filled and empty circles represent down-spin and up-spin Fe^{3+} sites, respectively. For each state, the expression of the total spin-exchange energy per hexamer ring is given, where N is the number of unpaired spins at each Fe^{3+} site (i.e., $N = 5$) and the four numbers in the square bracket from left to right are the relative energies in millielectronvolts per unit cell in the order of the entry given in Table 5.

energy $kT \sim J$, J can be estimated from the $I(T)$ measurements.[28] Because the double-integrated EPR intensity is proportional to the paramagnetic component of magnetic susceptibility χ, $I_{major}(T)$ and $I_{minor}(T)$ of $Ba_4KFe_3O_9$ could be fitted to the Curie–Weiss law[27] (cf. eq 4) to extract J_{nn} according to the molecular field theory (MFT; cf. eq 5)[27]

$$\frac{1}{\chi} = \frac{T - \theta}{C} \tag{4}$$

$$\theta = \frac{zJ_{nn}S(S+1)}{3k} \tag{5}$$

where θ is the Weiss constant, C is the Curie constant, and z (=2 for our Fe_6 clusters) is the number of nearest neighbors. The solid lines in Figure 8b are the best fits to eq 4 with parameters shown in Table 4 along with the J_{nn} values obtained from the MFT relationship shown in eq 5.

It is worth noting that the spin-exchange integral ratio $J_{nn}(minor)/J_{nn}(major) \sim 3-3.5$, determined from the $1/I$ vs T plot as well as the AW model, correlates well with the observed linewidth ratio $\delta B_{pp}(major)/\delta B_{pp}(minor) \sim 3.6$. Indeed, if all of the parameters of the AW theory are the same with the exception of J_{nn}, then $\delta B_{pp} \sim 1/J_{nn} \sim 1/\theta$. Thus, the major difference in the two magnetic environments corresponding to the narrow and broad EPR components is likely to be in the spin-exchange J_{nn} integral, with the rest of the parameters being about the same. We speculate that the observed discrepancy in J_{nn} obtained from the AW theory and the Curie–Weiss fits is due to either the assumptions i–iv adapted for our Fe_6 clusters or the inherent simplifications of the AW model. In fact, $(\delta B_{pp})_{observed}/(\delta B_{pp})_{calculated} \sim 2$ was expected by the authors of the AW model[31] and noticed in other experiments.[32] Authors in ref 32 attributed this discrepancy to the truncated Lorentzian line shape employed in the AW theory. We also note that the AW theory neglects the partial averaging of the dipolar fields due to spin flips on the time scale of the EPR experiment.

Spin-Exchange Interactions. To better understand the magnetic properties of $Ba_4KFe_3O_9$, we examined the spin-exchange interactions within the iron hexamer ring by performing energy-mapping analysis based on DFT electronic band structure calculations.[33–35] Because the cation disorder was observed for some positions of barium/potassium, we assumed an ordered stoichiometric arrangement of barium/potassium for our calculations by arranging them with the largest distance from each other, unless the occupancies of their positions are higher than

Table 5. Values in K of the Spin-Exchange Parameters J_{nn} and J_{nnn} Obtained from GGA+U Calculations for the Experimental (Exp) and Optimized (Opt) Crystal Structures of $Ba_4KFe_3O_9$

U (eV)	structure	k points	J_{nn}	J_{nnn}
0	exp	Γ	−347	−5.3
3	exp	Γ	−206	−0.9
3	exp	2 × 2 × 2	−207	−1.3
3	opt	2 × 2 × 2	−199	−1.0

0.9. Only the intraring spin-exchange interactions were considered, namely, the nearest-neighbor (J_{nn}) and next-nearest-neighbor (J_{nnn}) exchanges within each iron hexamer, while the interring spin-exchange interactions are expected to be negligible. To further simplify our discussion, it was assumed that all of the nearest-neighbor interactions J_{nn} are identical and so are the next-nearest-neighbor interactions J_{nnn}.

To determine the values of J_{nn} and J_{nnn}, we first consider the relative energies of the three ordered spin states (AF1, AF2, and AF3) of each iron hexamer ring shown in Figure 10 on the basis of DFT calculations. The calculations employed the projector-augmented wave method encoded in the VASP code[36] with the generalized-gradient approximation (GGA)[37] for the exchange-correlation functional, a plane-wave cutoff energy of 485 eV, and either a set of 2 × 2 × 2 k points or one k point (i.e., Γ point). To consider the electron correlation associated with Fe 3d states, GGA plus on-site repulsion (GGA+U) calculations[38] with U = 3 eV were also carried out. In evaluations of J_{nn} and J_{nnn}, the optimized crystal structure of $Ba_4KFe_3O_9$ was employed. With the lattice parameters kept constant, the atomic positions of $Ba_4KFe_3O_9$ were relaxed by GGA+U calculations (with U = 3 eV) using the AF1 state until the force acting on each ion is reduced below 0.01 eV/Å.

The relative energies of the AF1, AF2, and AF3 states obtained from our GGA+U calculations are summarized in Figure 10. The total spin-exchange energies of these states, per hexamer ring, can be expressed in terms of the spin Hamiltonian $\hat{H} = -\Sigma_{i<j}J_{ij}\hat{S}_i \cdot \hat{S}_j$, where $J_{ij} = J_{nn}$ and J_{nnn}. Through application of the energy expressions obtained for spin dimers with N unpaired spins per spin site (in the present case, $N = 5$),[39] the total spin-exchange energies of the three ordered spin states per 6-membered ring are written as summarized in Figure 10. Therefore, we determine J_{nn} and J_{nnn} by mapping the relative energies of the three ordered states obtained from the GGA+U calculations onto those expected from the total spin-exchange energies (Table 5).

In all cases, J_{nn} is strongly antiferromagnetic (on the order of −200 K), and J_{nnn} is negligible. It should be noted that, because $S = {}^5/_2$ for the high-spin Fe^{3+} ions, the effective nearest-neighbor spin exchange is given by $J'_{nn} = S^2J_{nn} = 25J_{nn}/4$. The width of the magnetic energy spectrum of $Ba_4KFe_3O_9$ scales as J'_{nn} and hence should spread over a wide range of energy. Then, even at room temperature, the Boltzmann distribution favors the occupation of lower-lying magnetic states in which more spins are paired, resulting in lower moments. Consequently, the effective magnetic moment calculated from χT will be much smaller than expected from the paramagnetic state in which all of the allowed magnetic states are equally occupied. As a result, the effective moment calculated from χT decreases continuously with a decrease of the temperature. In general, this kind of observation should be expected not only for magnetic oxides made up of corner-sharing FeO_4

tetrahedra with Fe^{3+} ($S = {}^5/_2$) ions but also for those made up of corner-sharing CoO_4 tetrahedra with Co^{4+} ($S = {}^5/_2$) ions, as found for Cs_2CoO_3, Rb_2CoO_3, and K_2CoO_3.[25]

The value of $J_{nn} \approx -200$ K obtained from the present GGA+U calculations is stronger than $J_{nn} \approx -20$ K for the major component estimated from the EPR measurements by an order of magnitude. In general, GGA+U electronic structure calculations overestimate the magnitude of spin-exchange interactions by a factor of up to 4−5.[34,35,40] Thus, we cannot exclude the possibility that our EPR analysis underestimated the value of J_{nn} by a factor of 2 or greater.

CONCLUSION

In summary, a new ferrite containing discrete 6-membered rings of FeO_4 tetrahedra has been synthesized and characterized experimentally and theoretically. In spite of the relatively short Fe−O−Fe contacts, no evidence of long-range magnetic order has been found in the magnetic susceptibility, Mössbauer, or heat capacity data. X-band EPR indicated the presence of two different magnetic species, with the Fe_6 clusters in $Ba_4KFe_3O_9$ accounting for ∼90% of the total spin count. The temperature dependence of the EPR signal intensity of the Fe_6 clusters is analyzed in terms of the Curie−Weiss law, yielding a Weiss constant of ∼−125 K. This corresponds to the spin-exchange integral J_{nn} of ∼−20 K, which agrees well with $|J_{nn}| \sim 12$ K estimated from the AW EPR line-shape theory. Our DFT calculations reveal that all nearest-neighbor magnetic interactions are strongly antiferromagnetic, while next-nearest-neighbor interactions are negligible. The lower than expected effective magnetic moment calculated from χT is explained as resulting from the occupation of lower-lying magnetic states in which more spins are paired, resulting in a lower moment.

ASSOCIATED CONTENT

Supporting Information. X-ray crystallographic data in CIF format. This material is available free of charge via the Internet at http://pubs.acs.org.

AUTHOR INFORMATION

Corresponding Author
*E-mail: zurloye@mail.chem.sc.edu.

ACKNOWLEDGMENT

Financial support from the National Science Foundation through Grants DMR0804209 and DMR0706593 is gratefully acknowledged. W.-J.S. and M.-H.W. acknowledge support from the Office of Basic Energy Sciences, Division of Materials Sciences, U.S. Department of Energy, under Grant DE-FG02-86ER45259, and also from the computing resources of the NERSC center and the HPC center of NCSU. EPR instrumentation was supported by Grants NIH S10RR023614, NSF CHE-0840501, and NCBC 2009-IDG-1015. S.N. and A.I.S. thank the U.S. Department of Energy's Office of Basic Energy Sciences for financial support (Grant DE-FG02-02ER15354). T.M.P. is grateful for support by UNF's Terry Presidential Professorship.

REFERENCES

(1) Deer, W. A.; Howie, R. A.; Zussman, J. *Rock Forming Minerals*; John Wiley & Sons: New York, 1986.
(2) Medina, M. E.; Iglesias, M.; Snejko, N.; Gutierrez-Puebla, E.; Monge, M. A. *Chem. Mater.* **2004**, *16*, 594.
(3) Ali, N. Z.; Nuss, J.; Sheptyakov, D.; Jansen, M. *J. Solid State Chem.* **2010**, 752.
(4) Brachtel, G.; Hoppe, R. *Angew. Chem., Int. Ed.* **1977**, *16*, 43.
(5) Zhou, H. D.; Lumata, L. L.; Kuhns, P. L.; Reyes, A. P.; Choi, E. S.; Dalal, N. S.; Lu, J.; Jo, Y. J.; Baicas, L.; Brooks, J. S.; Wiebe, C. R. *Chem. Mater.* **2009**, *21*, 156.
(6) Amann, P.; Sobotka, B. M.; Fastje, O.; Moller, A. *Z. Anorg. Allg. Chem.* **2007**, *633*, 2579.
(7) Delattre, J. L. *Chemistry* **2002**, 143.
(8) Hoshino, N.; Ako, A. M.; Powell, A. K.; Oshio, H. *Inorg. Chem.* **2009**, *48*, 3396. Müller, A.; Peters, F.; Pope, M. T.; Gatteschi, D. *Chem. Rev.* **1998**, *98*, 239.
(9) Hoffman, R. *Sci. Am.* **1993**, *268*, 66. Kortz, U.; Müller, A.; van Slageren, J.; Schnack, J.; Dalaf, N. S.; Dressel, M. *Coord. Chem. Rev.* **2009**, *253*, 2315.
(10) Beck, J. S.; Vartuli, J. C. *Curr. Opin. Solid State Mater. Sci.* **1996**, *1*, 76.Breck, D. W. *Zeolite Molecular Sieves*; John Wiley: New York, 1974.
(11) Benelli, C.; Parsons, S.; Solan, G. A.; Winpenny, R. E. P. *Angew. Chem.* **1996**, *108*, 1967. Caneschi, A.; Cornia, A.; Fabretti, A. C.; Foner, S.; Gatteschi, D.; Grandi, R.; Schenetti, L. *Chem.—Eur. J.* **1996**, *11*, 1379.
(12) Taft, K. L.; Delfs, C. D.; Papaefthymiou, G. C.; Foner, S.; Gatteschi, D.; Lippard, S. J. *J. Am. Chem. Soc.* **1994**, *116*, 823.
(13) Taft, K. L.; Lippard, S. J. *J. Am. Chem. Soc.* **1990**, *112*, 9629.
(14) Baca, S. G.; Speldrich, M.; Ellern, A.; Kögerler, P. *Materials* **2011**, *4*, 300–310.
(15) Watton, S. P.; Fuhrmann, P.; Pence, L. E.; Caneschi, A.; Corina, A.; Abbati, G. L.; Lippard, S. J. *Angew. Chem., Int. Ed.* **1997**, *36*, 2774.
(16) Giaquinta, D. M.; Davis, W. M.; zur Loye, H.-C. *Acta Crystallogr.* **1994**, *C50*, 5–7. Mwamuka, J. N.; Gemmill, W. R.; Stitzer, K. E.; Smith, M. D.; zur Loye, H.-C. *J. Alloys Compd.* **2004**, *377*, 91–97. Gemmill, W. R.; Smith, M. D.; zur Loye, H.-C. *Solid State Sci.* **2007**, *9*, 380–384. Roof, I. P.; Smith, M. D.; zur Loye, H.-C. *Solid State Sci.* **2010**, *12*, 1211–1214. Zhao, Q.; Smith, M. D.; zur Loye, H.-C. *J. Chem. Crystallogr.* **2011**in press.
(17) Giaquinta, D. M.; Papaefthymiou, G. C.; zur Loye, H.-C. *J. Solid State Chem.* **1995**, *114*, 199.
(18) Mugavero, S. J., III; Gemmill, W. R.; Roof, I. P.; zur Loye, H.-C. *J. Solid State Chem.* **2009**, *182*, 1950–1963. Bugaris, D. E.; zur Loye, H.-C. *Angew. Chem., Int. Ed.* **2011**in press.
(19) Delattre, J. L.; Stacy, A. M. *J. Solid State Chem.* **2003**, *172*, 261.
(20) *SMART*, version 5.625; *SAINT+*, version 6.45; *SADABS*, version 2.05; Bruker Analytical X-ray Systems, Inc.: Madison, WI, 2001.
(21) Sheldrick, G. M. *Acta. Crystallogr., Sect. A* **2008**, *64*, 112.
(22) Spek, A. L. *PLATON, A Multipurpose Crystallographic Tool*; Utrecht University: Utrecht, The Netherlands, 1998.
(23) Smirnov, A. I.; Belford, R. L. *J. Magn. Reson. A* **1995**, *113*, 65.
(24) Smirnov, A. I.; Smirnova, T. I. *Biol. Magn. Reson.* **2004**, *21*, 277.
(25) Nuss, J.; Ali, N. Z.; Jansen, M. *Acta Crystallogr.* **2007**, *B63*, 719.
(26) Jansen, M.; Hoppe, R. *Z. Anorg. Allg. Chem.* **1974**, *408*, 75.
(27) Carlin, R. L. *Magnetochemistry*; Springer-Verlag: New York, 1986.
(28) Abragam, A.; Bleaney, B. *Electron Paramgnetic Resonance of Transition Ions*; Dover Publications: New York, 1986.
(29) Smirnova, T. I.; Smirnov, A. I.; Belford, R. L.; Clarkson, R. B. *J. Am. Chem. Soc.* **1998**, *120*, 5060.
(30) Smirnov, A. I.; Sen, S. *J. Chem. Phys.* **2001**, *115*, 7650.
(31) Anderson, P. W.; Weiss, P. R. *Rev. Mod. Phys.* **1953**, *25*, 269.
(32) Dalal, N. S.; Millar, J. M.; Jagadeesh, M. S.; Seehra, M. S. *J. Chem. Phys.* **1981**, *74*, 1916. Gulley, J. E.; Hone, D.; Scapino, D. J.; Silbernagel, B. G. *Phys. Rev. B* **1970**, *1*, 1020.
(33) Whangbo, M.-H.; Koo, H.-J.; Dai, D. *J. Solid State Chem.* **2003**, *176*, 417.
(34) Koo, H. J.; Whangbo, M.-H. *Inorg. Chem.* **2008**, *47*, 4779.
(35) Koo, H. J.; Whangbo, M.-H. *Inorg. Chem.* **2008**, *47*, 128.

(36) Kresse, G.; Hafner, J. *Phys. Rev. B* **1993**, *47*, 558. Kresse, G.; Furthmüller, J. *Comput. Mater. Sci.* **1996**, *6*, 15. Kresse, G.; Furthmüller, J. *Phys. Rev. B* **1996**, *54*, 11169.
(37) Perdew, J. P.; Burke, K.; Ernzerhof, M. *Phys. Rev. Lett.* **1996**, *77*, 3865.
(38) Dudarev, S. L.; Botton, G. A.; Savrasov, S. Y.; Humhreys, C. J.; Shutton, A. P. *Phys. Rev. B* **1998**, *57*, 1505.
(39) Dai, D.; Whangbo, M.-H. *J. Chem. Phys.* **2001**, *114*, 2887. Dai, D.; Whangbo, M.-H. *J. Chem. Phys.* **2003**, *118*, 29.
(40) Xiang, H. J.; Lee, C.; Whangbo, M.-H. *Phys. Rev. B* **2007**, *76*, 220411.